CHAPTER 260

Wind-Induced Waves and Currents in a Nearshore Zone

Nobuhiro Matsunaga[1], Misao Hashida[2] and Hiroshi Kawakami[3]

Abstract

Characteristics of waves and currents induced when a strong wind blows shoreward in a nearshore zone have been investigated experimentally. The drag coefficient of wavy surface has been related to the ratio u_{*a}/c_p, where u_{*a} is the air friction velocity on the water surface and c_p the phase velocity of the predominant wind waves. Though the relation between the frequencies of the predominant waves and fetch is very similar to that for deep water, the fetch-relation of the wave energy is a little complicated because of the wave shoaling and the wave breaking. The dependence of the energy spectra on the frequency f changes from f^{-5} to f^{-3} in the high frequency region with increase of the wind velocity. A strong onshore drift current forms along a thin layer near the water surface and the compensating offshore current is induced under this layer. As the wind velocity increases, the offshore current velocity increases and becomes much larger than the wave-induced mass transport velocity which is calculated from Longuet-Higgins' theoretical solution.

1. Introduction

When a nearshore zone is under swell weather conditions, the

1 Associate Professor, Department of Earth System Science and Technology, Kyushu University, Kasuga 816, Japan.
2 Professor, Department of Civil Engineering, Nippon Bunri University, Oita 870-03, Japan.
3 Graduate student, Department of Earth System Science and Technology, Kyushu University, Kasuga 816, Japan.

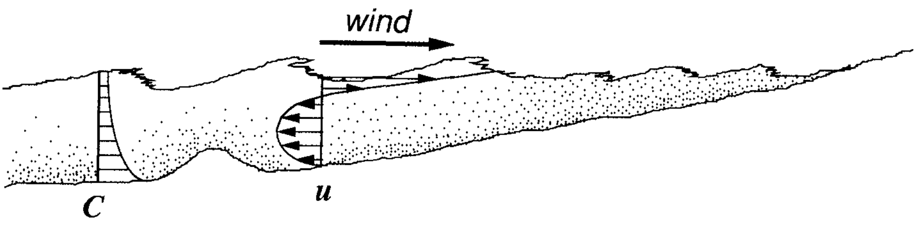

Fig.1 Sketch of sediment transport process in a nearshore zone under a storm.

sediment transport process depends strongly on the wave-induced mass transport velocity. The process is relatively slow. On the other hand, a large amount of sediment is suspended and transported under a storm. The transport process under storm weather conditions is very different from that under swell weather conditions. Shepard (1950) observed the change of beach profiles along Scripps Pier, La Jalla, Carifornia. He revealed that a beach profile with longshore bars forms under storm weather conditions and a profile with pronounced berms develops under swell weather conditions. The former has been referred to as the winter profile, and the latter as the summer profile. Komer (1976) claims the use of terms 'storm profile' and 'swell profile' to be preferable.

Many researchers (e.g., Johnson (1949), Rector (1954), Iwagaki and Noda (1963)) investigated seasonal variations of beach profiles and obtained a critical wave steepness at which they change from the storm profile to the swell one. In their studies, the steepness of storm waves was regarded as the most important factor to determine the beach profile. However, it seems to be difficult to explain the sediment transport process under storm weather conditions without considering the wind effect. In the case when a strong wind blows shoreward, a strong onshore wind-driven current forms along a thin layer near the water surface, and the compensating offshore current along the bed (see figure 1). The offshore current may transport a large amount of sediment seaward because the concentration of suspended sediment increases to the seabed. After a storm, in fact, we can often see a beach being eroded remarkably and floating matters such as seaweeds and pieces of wood being cast ashore.

In this study, waves and currents formed in a nearshore zone under storm weather conditions have been investigated experimentally in order to understand the wind effect on the onshore-offshore sediment transport.

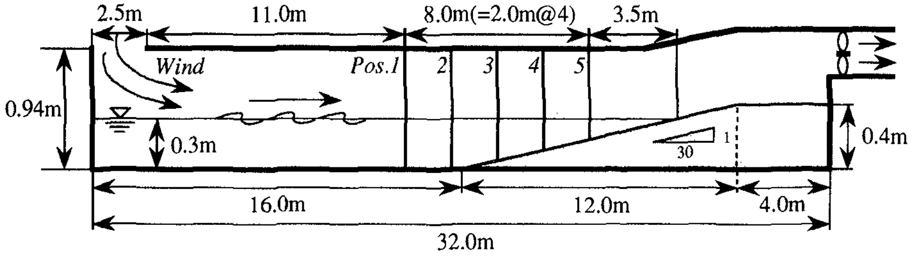

Fig.2 Experimental apparatus.

2. Experimental set-up

Experiments were carried out by using a water tank equipped with an inhalation-type wind tunnel. Figure 2 shows a schematic diagram of the experimental apparatus. The tank was 32 m long, 0.6 m wide and 0.94 m high. A sloping bed was attached to the end of the tank as a beach model. Its gradient was fixed at 1/30. The mean water depth was 0.3 m at the horizontal bed section. Wind waves were generated by the shoreward wind. Measurements of the wind velocity, wave height and wind-induced current velocity were made at positions 1 to 5. The distance from the intake of the wind to Position 1 was 11 m. The intervals between the adjacent measuring positions were 2.0 m. Positions 1 and 2 were in the horizontal bed section and positions 3 to 5 on the sloping bed. The wind velocity was measured by using a propeller-type current meter. In the wave height measurements, two capacitance-type wave gauges were used in order to obtain the phase velocity. They were set 28 cm away. The wave signals were digitized at the intervals of 1/50 s and 16,384 data were sampled. Horizontal and vertical components of the wind-induced currents were obtained by using an electromagnetic current meter. The sampling rate of the velocity signals was 1/20 s and the number of sampled data was 2,048.

Table 1 shows the wind parameters and the wave ones. Five tests in all were carried out by varing the wind velocity. The cross-sectionally averaged wind velocity U_m was varied from 7.60 m/s to 21.8 m/s. F is the fetch and h the mean water depth. The air friction velocity on the wavy surface is denoted by u_{*a} and the mean wind velocity at a 10 m height by U_{10}. H is the mean wave height. The periods, lengths and phase velocities of predominant waves are

Table 1 Experimental parameters.

U_m(m/s)	Pos.	F(m)	h(cm)	u_{*a}(m/s)	U_{10}(m/s)	H(cm)	T_p(s)	L_p(m)	c_p(m/s)	E(cm^2)	u_{*a}/c_p	C_D	U_r
7.60	1	11.0	30.0	0.335	10.9	2.20	0.467	0.400	0.856	0.688	0.391	9.45E-4	0.130
	2	13.0	30.0	0.259	10.4	2.43	0.467	0.417	0.893	0.836	0.290	6.20E-4	0.157
	3	15.0	25.0	0.274	10.4	2.63	0.474	0.433	0.914	0.977	0.300	6.94E-4	0.316
	4	17.0	18.4	0.238	10.7	2.83	0.515	0.493	0.956	1.17	0.249	4.95E-4	1.10
	5	19.0	11.9	0.294	11.1	2.99	0.535	0.483	0.903	1.26	0.326	7.02E-4	4.14
11.6	1	11.0	30.4	0.682	18.1	4.68	0.585	0.637	1.09	2.88	0.626	1.42E-3	0.676
	2	13.0	30.2	0.568	17.3	5.06	0.595	0.685	1.15	3.31	0.494	1.08E-3	0.862
	3	15.0	25.2	0.723	19.1	5.30	0.658	0.743	1.13	3.53	0.640	1.44E-3	1.83
	4	17.0	18.7	0.823	20.6	5.33	0.662	0.834	1.26	3.59	0.653	1.60E-3	5.67
	5	19.0	12.4	0.658	19.1	4.46	0.699	0.741	1.06	2.57	0.621	1.19E-3	12.8
15.5	1	11.0	29.9	1.18	26.4	5.58	0.662	0.768	1.16	4.01	1.02	2.00E-3	1.23
	2	13.0	30.1	1.29	28.0	6.41	0.714	0.971	1.36	5.07	0.949	2.10E-3	2.22
	3	15.0	25.5	1.19	27.3	6.55	0.709	0.851	1.20	5.26	0.992	1.91E-3	2.86
	4	17.0	19.3	1.32	29.1	6.11	0.746	0.896	1.20	4.86	1.10	2.06E-3	6.82
	5	19.0	13.4	1.49	31.1	4.55	0.775	0.791	1.02	3.01	1.46	2.30E-3	11.8
18.9	1	11.0	28.5	1.10	29.0	6.05	0.699	0.881	1.26	4.71	0.873	1.45E-3	2.03
	2	13.0	30.0	1.63	34.8	6.39	0.719	0.971	1.35	5.45	1.21	2.20E-3	2.23
	3	15.0	25.6	1.82	36.9	6.69	0.746	0.955	1.28	6.06	1.42	2.44E-3	3.64
	4	17.0	19.6	2.10	40.3	5.87	0.787	1.00	1.27	4.95	1.65	2.72E-3	7.80
	5	19.0	14.0	2.57	45.6	4.81	0.840	0.830	0.988	3.43	2.60	3.19E-3	12.1
21.8	1	11.0	27.8	1.99	39.4	6.30	0.719	0.971	1.35	5.38	1.47	2.54E-3	2.76
	2	13.0	28.1	2.04	43.3	6.49	0.741	1.02	1.38	5.92	1.48	2.21E-3	3.04
	3	15.0	24.1	2.02	42.9	6.91	0.794	1.04	1.31	6.41	1.54	2.21E-3	5.34
	4	17.0	18.2	2.19	45.1	5.76	0.794	1.02	1.28	4.64	1.71	2.36E-3	9.94
	5	19.0	13.5	2.40	45.9	4.19	0.885	1.04	1.18	3.09	2.03	2.72E-3	18.4

represented by T_p, L_p and c_p, respectively. E denotes the total wave energy. The drag coefficient C_D is defined by $(u_{*a}/U_{10})^2$, and U_r is an Ursell parameter defined by $HL_p{}^2/h^3$.

3. Experimental results and discussion

3.1 Drag coefficient of wavy surface

Vertical profiles of the mean wind velocity U in the case of U_m = 15.5 m/s are shown in figure 3, where z is the vertical coordinate taken upward from the mean water level. Though the wind velocity near the ceiling of the wind tunnel decreases due to the boundary layer, a logarithmic profile is formed near the water surface. The wind set-up increases the wind velocity and the velocity gradient near the water surface in the leeward direction. The values of u_{*a} were calculated by

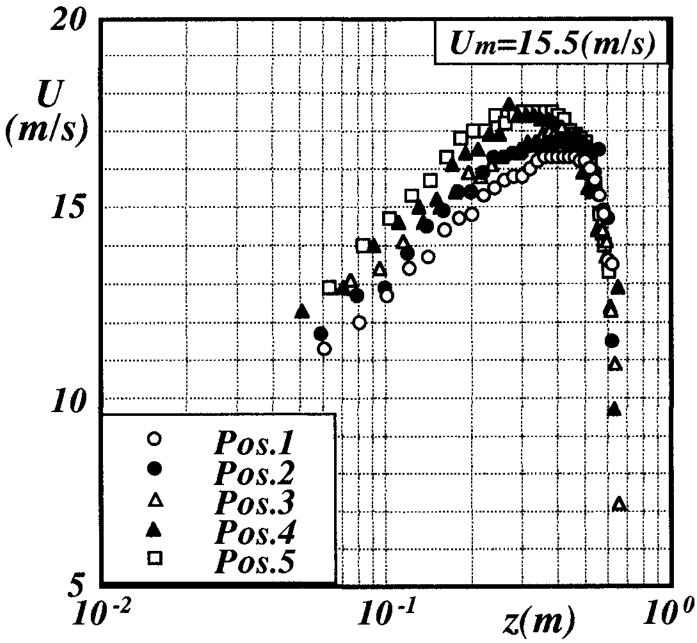

Fig.3 Vertical profiles of mean wind velocity.

fitting the logarithmic law

$$U = \frac{u_{*a}}{\kappa} \ln \frac{z}{z_0} \tag{1}$$

to the wind velocity profiles, where κ (= 0.4) is von Karman's constant. It is read from table 1 that the values of u_{*a} increase with increase of U_m and with increase of F. The drag coefficient C_D is defined by

$$C_D = \left(\frac{u_{*a}}{U_{10}}\right)^2 \tag{2}$$

The relation between C_D and U_{10} has been investigated until now by many researchers. Some of the empirical expressions and our experimental data are shown in figure 4. The data include ones obtained through other experiments in which the wind blew on swells made by a wavemaker. Though the U_{10}-dependence for the wind waves is different from that for the swell and wind waves, the data approach gradually to Kondo's empirical curve when $U_{10} \geq 25$ m/s. Some of our data are under the values to which the empirical curves

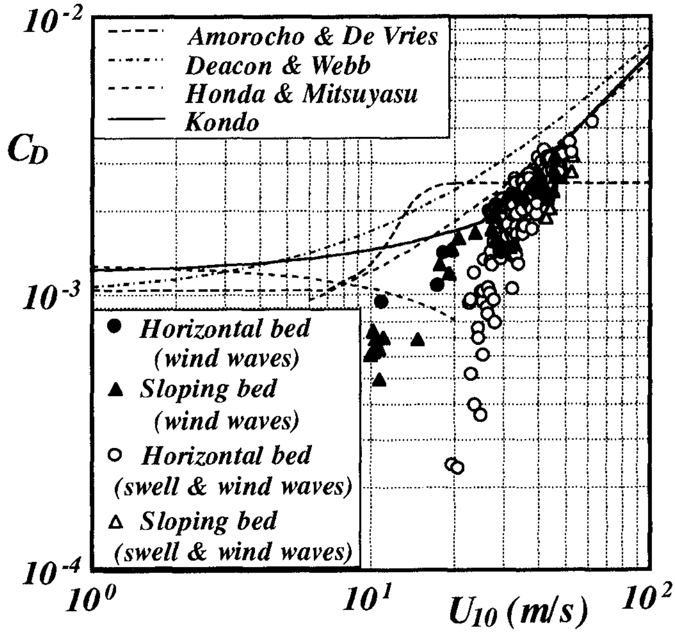

Fig.4 U_{10}-dependence of C_D.

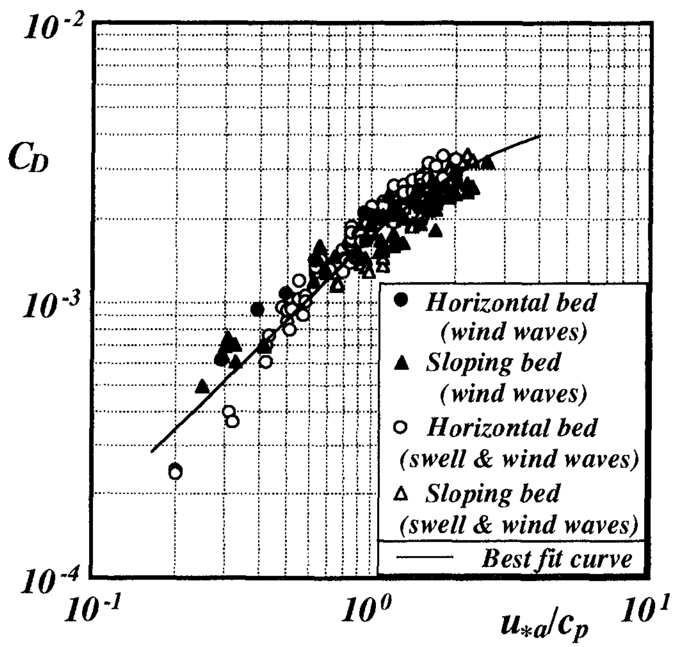

Fig.5 Relation between C_D and u_{*a}/c_p.

approach with increase of U_{10}. The validity of these data remains to be proved.

The relation of C_D and U_{10} has been investigated from the standpoint of practicality. However, if we try to obtain a universal form for C_D, relations between C_D and dimensionless parameters should be examined. Figure 5 shows a relation between C_D and u_{*a}/c_p. The solid line is drawn by the least-square fit method. The discrepancy between the data for the wind waves and ones for the swell and wind waves becomes much smaller than that shown in figure 4. Increasing linearly with u_{*a}/c_p when $u_{*a}/c_p \leq 1$, C_D becomes constant for a large value of u_{*a}/c_p.

3.2 Wind waves in shallow water

It is well-known that the energy of wind waves in deep water and the periods of the predominant wind waves increase with increase of u_{*a} and F. The empirical fetch-relations proposed by Mitsuyasu (1968) are

$$\frac{gE^{1/2}}{u_{*a}^2} = 1.31\times10^{-2}\left(\frac{gF}{u_{*a}^2}\right)^{0.504} \tag{3}$$

and

$$\frac{u_{*a} f_p}{g} = 1.00\left(\frac{gF}{u_{*a}^2}\right)^{-0.330} \tag{4}$$

where $f_p = 2\pi/T_p$. As read from table 1, the values of T_p in shallow water increase with increase of F but the values of E do not increase monotonically with F because of the wave breaking. We can also read that the increase of F corresponds to that of U_r. It means that the wind waves progress into a shallow region with increase of F. If equations (3) and (4) are rewritten by using the wave energy E_0 and the frequency f_{p0} at a standard point,

$$\frac{E}{E_0} = \left(\frac{F}{F_0}\right)^{1.008} \tag{5}$$

and

$$\frac{f_p}{f_{p0}} = \left(\frac{F}{F_0}\right)^{-0.330} \tag{6}$$

are obtained, where F_0 is fetch at the standard point. Equations (5) and (6) give the increasing rate of the wave energy to E_0 and the decreasing rate of the predominant wave frequency to f_{p0}, respectively. The

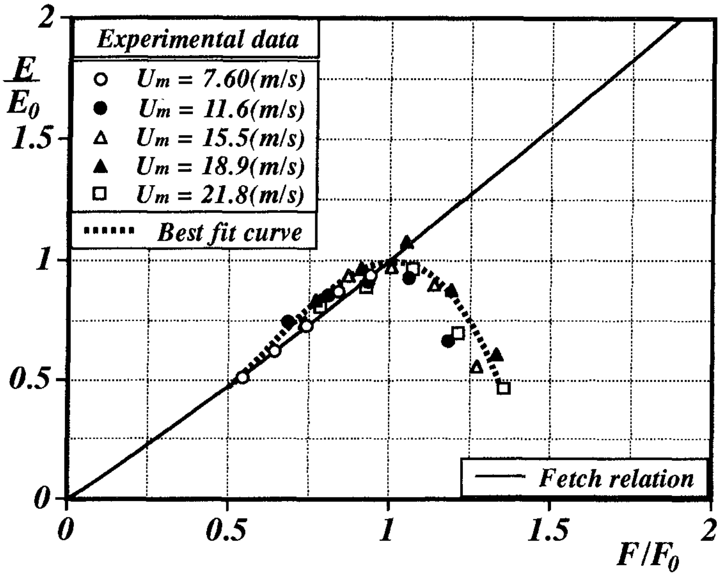

Fig.6 Comparison of fetch relation of E in shallow water with that in deep water.

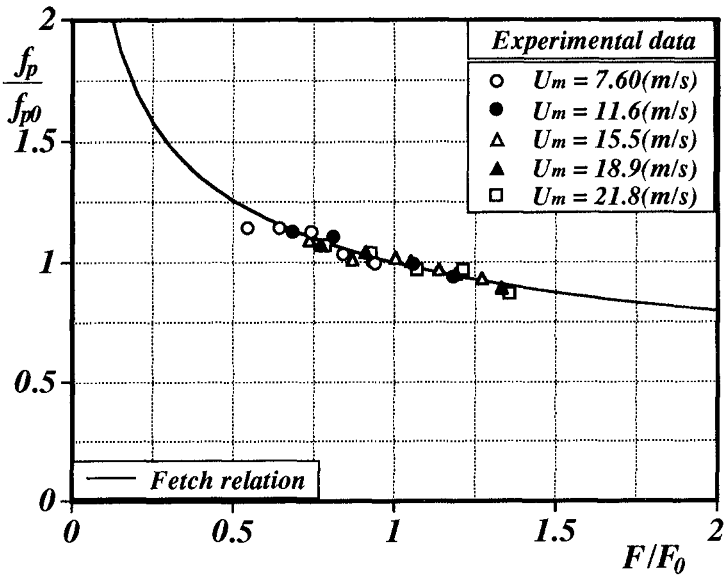

Fig.7 Comparison of fetch relation of f_p in shallow water with that in deep water.

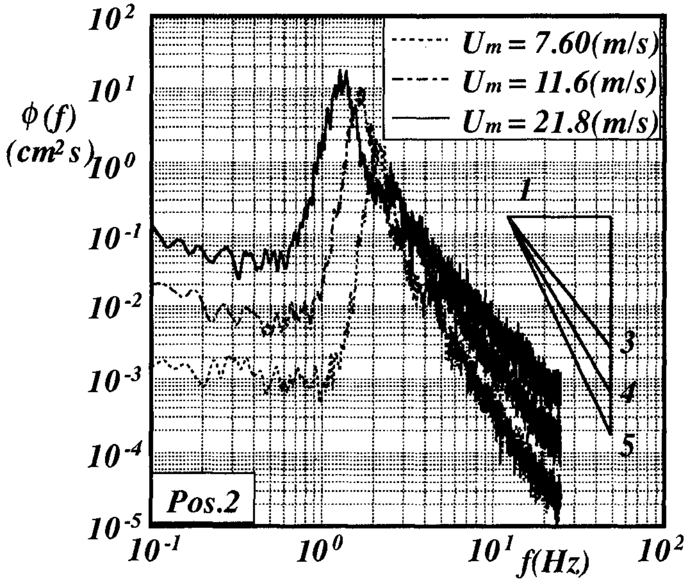

Fig.8 Variation of energy spectra of wind waves with increase of U_m.

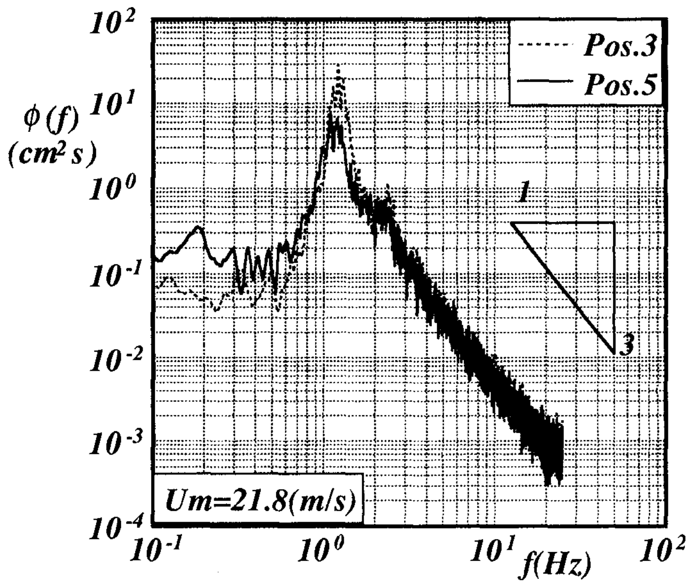

Fig.9 Comparison between energy spectra before and behind breaking point.

values of E/E_0 are plotted against F/F_0 in figure 6, where the fetch to the breaking point is selected as F_0. The breaking point of the wind waves is defined as a position at which E becomes maximum. The solid line expresses the relation given by equation (5). The dashed line is the best fit curve based on the data. In the offshore side from the breaking point (F/F_0 < 1), the increasing rate of E is a little larger than that in deep water. It may be caused by the wave shoaling. On the other hand, in the onshore side (F/F_0 > 1), the increasing rate decreases rapidly with fetch because of the wave breaking. Figure 7 shows the relation between f_p/f_{p0} and F/F_0. The data collapse well onto the curve given by equation (6). It means that the decreasing rate of f_p in shallow water agrees well with that in deep water.

Figure 8 shows energy spectra $\phi(f)$ of wind waves measured at Position 2. The total energy increases with increase of U_m because no wave breaking occurs at Position 2. The values of $\phi(f_p)$ become large with the U_m-increase and the values of f_p become small. These are the same features as in deep water waves. The f-dependence of $\phi(f)$ in the high frequency region changes from f^{-5} to f^{-3} as the wind velocity increases. The spectral form in an equilibrium region is given by

$$\phi(f) \propto g^{\alpha} u_{*a}^{2-\alpha} f^{-3-\alpha} \tag{7}$$

with the aid of a dimensional analysis, where g is the gravity acceleration and α an arbitrary constant. In the case when the effect of the gravity is much larger than the wind effect, α takes 2. At that time, $\phi(f)$ is proportional to f^{-5} in the high frequency region. On the other hand, as the wind velocity increases, it can be guessed that the effect of the gravity becomes small and $\phi(f) \propto f^{-3}$ in the limit. These dimensional considerations are supported by the results shown in figure 8.

Figure 9 shows the energy spectra of wind waves at positions 1 to 5. It is seen that the energy of the predominant waves decays remarkably due to the wave breaking.

3.3 Wind-induced currents

Figures 10 (a) to (e) show vertical profiles of wind-induced currents. Here, u is the horizontal component of the current velocity and the negative value indicates that the current is offshore. The vertical axis z is normalized using the local water depth h. Offshore wind-induced currents are formed in the range of $-1.0 \le z/h \le -0.1$. This suggests that an onshore strong current is generated in a thin layer near the water surface. As a natural result, the offshore currents

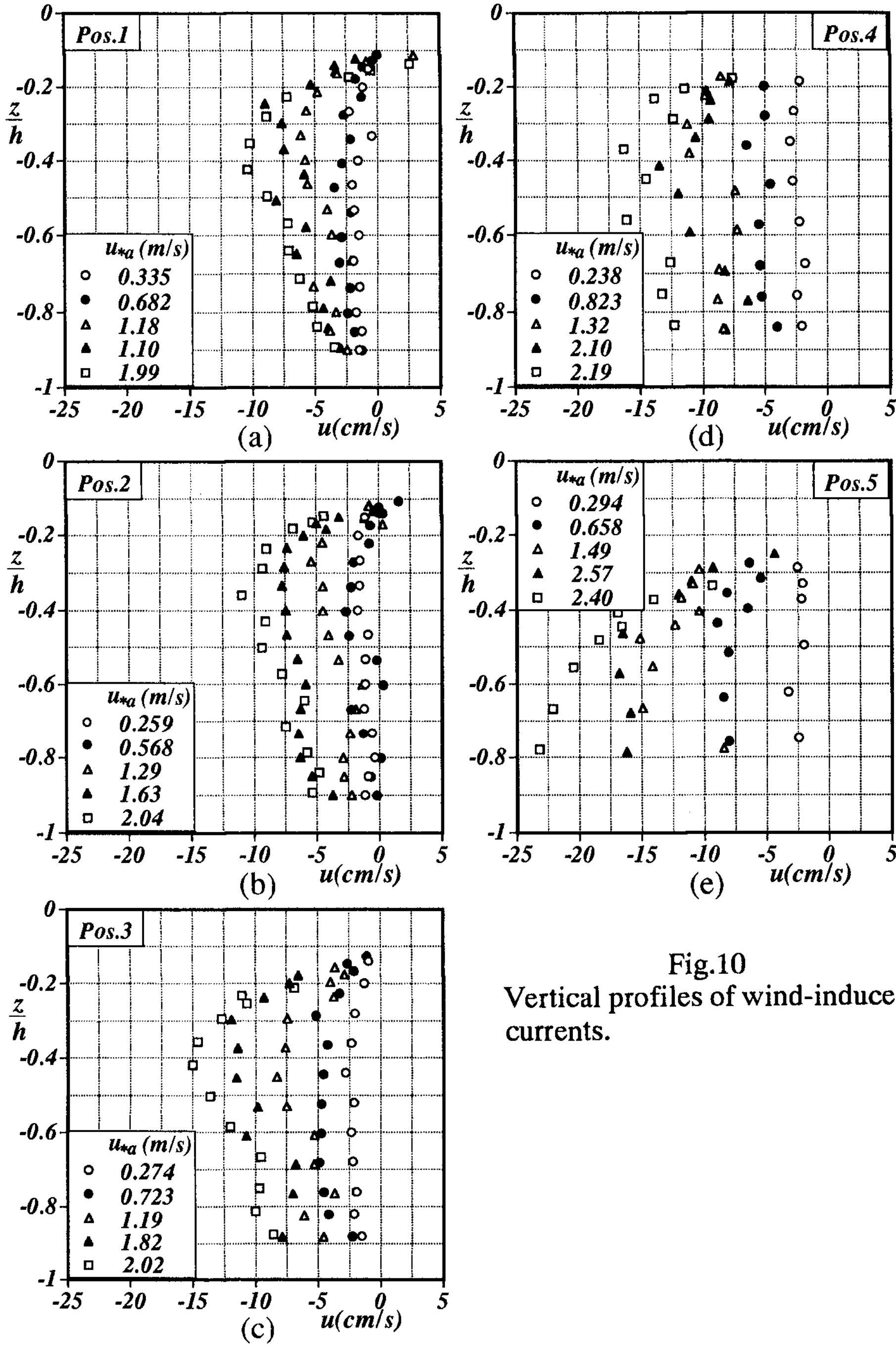

Fig.10
Vertical profiles of wind-induced currents.

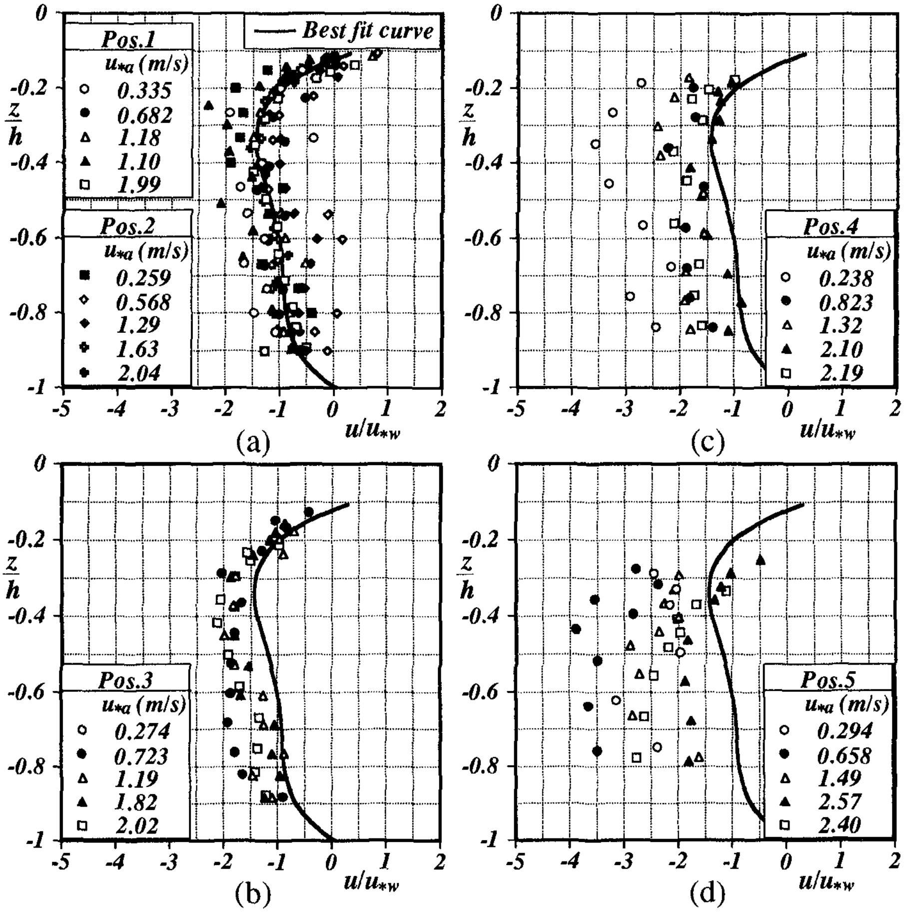

Fig.11 Normalized vertical profiles of wind-induced currents.

become stronger as u_{*a} increases and as the water depth decreases.

In figures 11 (a) to (d), the values of u are normalized by using the water friction velocity u_{*w} calculated from $(\rho_a/\rho_w)^{1/2}u_{*a}$. Here ρ_a and ρ_w are the densities of air and water, respectively. The values of u/u_{*w} at positions 1 and 2 are expressed approximately by the solid line (see figure 11 (a)). It may be due to that the wind-induced currents on a horizontal bed are uniform in the flow direction and the current velocity increases in proportion to u_{*a}. The maximum velocity of the offshore currents takes about $1.5u_{*w}$ at z/h = -0.3. Figures 11 (b) to (d) show the normalized vertical profiles for positions 3 to 5, respectively. The solid lines in these figures are the one drawn in figure 11 (a). It is

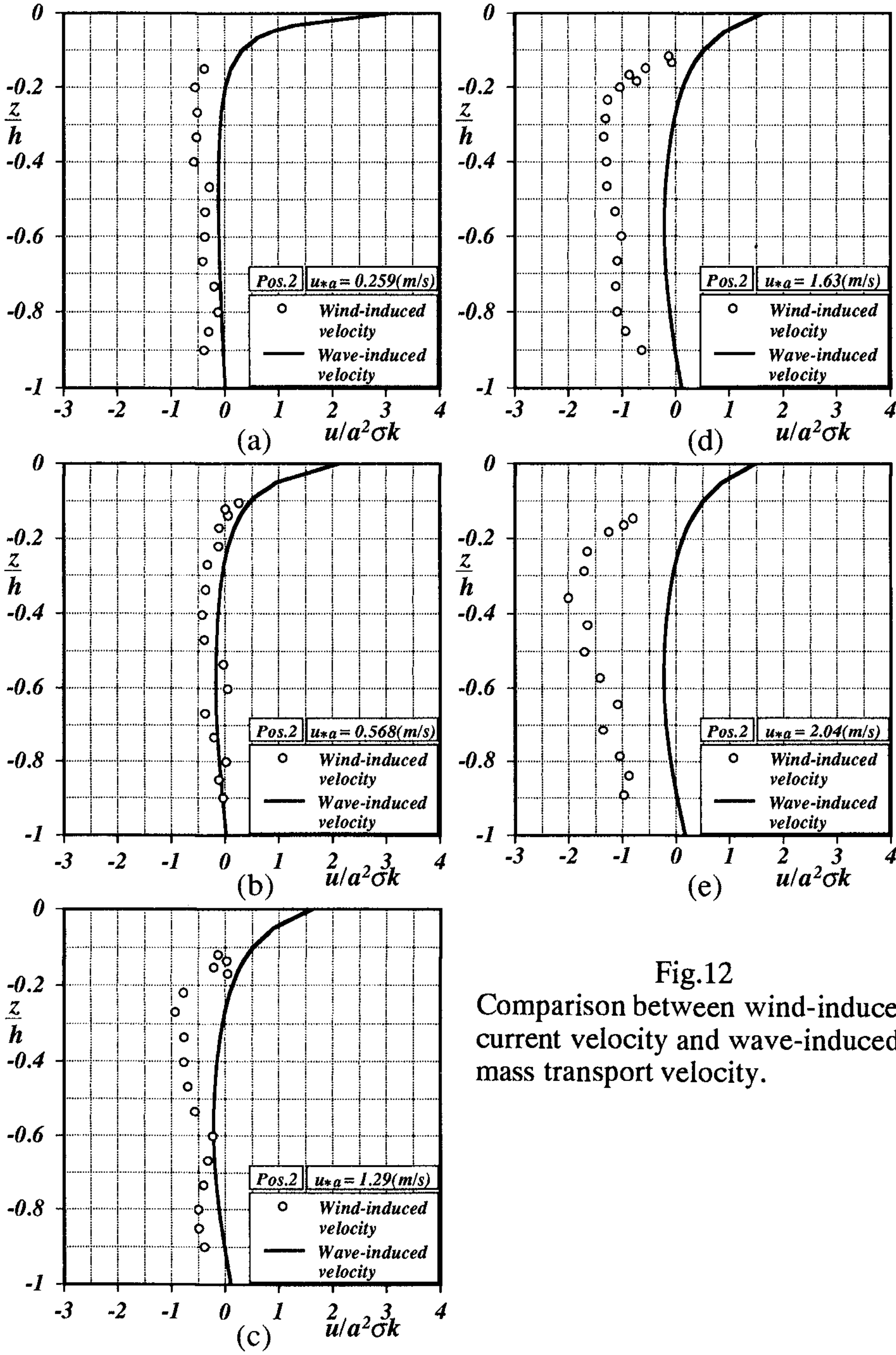

Fig.12
Comparison between wind-induced current velocity and wave-induced mass transport velocity.

difficult to express universally the vertical profiles on the sloping bed by using u_{*w} and h, because even if u_{*w} is uniform in the leeward direction, the water depth variation makes the offshore currents accelerate. In fact, the values of u/u_{*w} increase in the leeward direction.

Dimensionless velocity profiles of the wind-induced currents at Position 2 and the wave-induced currents are compared in figures 12 (a) to (e). The wave-induced velocity is estimated by using Longuet-Higgins' theoretical solution (Longuet-Higgins (1953)) and the measured values at Position 2. The theoretical results are drawn by the solid lines. The wave amplitude a, frequency σ and wave number k are given by $H/2$, $2\pi/T_p$ and $2\pi/L_p$, respectively. From these figures, it is seen that the wind-induced currents become much larger than the wave-induced currents as the values of u_{*w} increase. This suggests that the wind effect on the sediment transport under storm weather conditions is very important rather than the increase of wave steepness.

4. Conclusions

In this study, the caracteristics of waves and currents formed in a nearshore zone under storm weather conditions have been investigated experimentally. The obtained main results are as follows.

1) The drag coefficient of wavy surface C_D is related to u_{*a}/c_p. The values of C_D increase monotonically with increase of u_{*a}/c_p but become constant for a large value of u_{*a}/c_p.

2) In the offshore side from the breaking point, the increasing rate of the total wave energy in shallow water is a little larger than that in deep water because of the wave shoaling. However, the increasing rate reduces remarkably in the onshore side from the breaking point due to the wave breaking. The decreasing rate of the predominant wave frequency in shallow water agree well with that in deep water.

3) The wind-induced current velocity increases with the wind velocity and becomes much larger than the wave-induced current velocity. Therefore, the wind effect is very important in the sediment transport process under storm weather conditions.

The authors are grateful for a grant from the Ministry of Education, Science and Culture.

References

Iwagaki, Y. and Noda, H. (1963) Laboratory study of scale effects in two-dimensional beach processes, Proc. 8th Conf. on Coastal Eng., ASCE, 194 - 210.

Johnson, J.W. (1949) Scale effects in hydraulic models involving wave motion, Trans. Am. Geophys. Union **30**, 517 - 525.

Komar, P.D. (1976) Beach processes and sedimentation, Prentice-Hall, Englewood Cliffs, N.J., 288 - 300.

Longuet-Higgins, M.S. (1953) Mass transport in water waves, Phil. Trans. Roy. Soc. (London), series A, **245**, 535 - 581.

Rector, R.L. (1954) Laboratory study of the equilibrium profiles of beaches, U.S. Army Corps of Engrs., Beach Erosion Board Tech. Memo., **41**.

Shepard, F.P. (1950) Beach cycles in Southern California, U.S. Army Corps of Engrs., Beach Erosion Board Tech. Memo., **20**.